ACTA METALLURGICA SLOVACA
2024, VOL. 30, NO. 1, 34-40

RESEARCH PAPER

CORROSION EVALUATION OF SUPER DUPLEX STAINLESS STEEL MADE BY LPBF

Mengistu Dagnaw[1], Zbigniew Brytan[1], Jana Bidulská[2], Róbert Bidulský[3,4]*

[1]Department of Engineering Materials and Biomaterials, Faculty of Mechanical Engineering, Silesian University of Technology, Konarsiego 18a, 44-100, Gliwice, Poland
[2]Department of Plastic Deformation and Simulation Processes, Institute of Materials and Quality Engineering, Faculty of Materials, Metallurgy and Recycling, Technical University of Kosice, Letná 9/A, 04200 Kosice, Slovakia
[3]Bodva Industry and Innovation Cluster, Budulov 174, 04501 Moldava nad Bodvou, Slovakia
[4]Advanced Research and Innovation Hub, Budulov 174, 04501 Moldava nad Bodvou, Slovakia

*Corresponding author: mengistu.jemberu.dagnaw@polsl.pl

Received: 31.01.2024
Accepted: 17.02.2024

ABSTRACT

This study investigated the electrochemical corrosion performance of printed and heat-treated 2507 Super Duplex Stainless Steel (SDSS). The corrosion was studied by Tafel polarization and electrochemical impedance spectroscopy (EIS) methods in a 3.5% NaCl solution. For this purpose, the as-built and heat-treated printed samples (solution annealed and stress-relieved) were examined by LOM/SEM and X-ray diffraction to evaluate the phase changes of steel at different processing stages. The correlation between corrosion resistance, structure, and heat treatment was assessed. As a result of the very fast cooling rate of the laser powder bed fusion (LPBF) process, SDSS reveals ferrite as the major phase in the printed samples. The ferrite grains are elongated in the build direction, with some austenite precipitation along the grain boundaries or as Widmanstatten laths. Because the ferrite phase's corrosion potential is lower than that of austenite, corrosion preferentially proceeds in the steel matrix. For this reason, balancing the two-phase structure or reducing residual stresses after the printing process has a positive effect on improving the corrosion resistance of duplex stainless steel produced by LPBF. The stress-relieved and as-printed SDSS exhibits reduced corrosion characteristics by around 20% compared to the solution-annealed SDSS, according to anodic polarization curves. Based on EIS results, the solution-annealed SDSS revealed an almost double increase in corrosion resistance (based on charge transfer resistance values) compared to the as-printed and stress-relieved conditions.

Keywords: Duplex stainless steel, Super Duplex Stainless Steel, Laser Powder Bed Fusion, Corrosion, Tafel polarization, EIS.

INTRODUCTION

Additive manufacturing is a pivotal technology that facilitates the production of intricate shapes with little geometric constraints, in contrast to conventional manufacturing methods. Currently, the production of intricate components, particularly those composed of challenging metallic alloys, poses a significant obstacle within the manufacturing domain. The utilization of additive manufacturing (AM) technology is presently seen as a highly promising approach to address these difficulties, presenting an area of research that is relatively unexplored for metallurgists and process engineers. Additive manufacturing (AM) technologies have emerged as a very stimulating breakthrough, particularly in the realm of component design. These processes have allowed the production of components that were previously unattainable using standard manufacturing methods [1-3].
The laser powder bed fusion technique (LPBF), sometimes known as selective laser melting (SLM), employs a laser beam to selectively liquefy thin layers of metal powder, resulting in the gradual formation of homogeneous metal objects through layer-by-layer fabrication. Laser powder bed fusion (LPBF) is a prevalent additive manufacturing technique utilized extensively in industrial settings for the production of metal components [4, 5].

Additive manufacturing development is exponentially accelerating cost adjustment and efficiency in producing different components for a wide range of applications. The reduction in energy of up to 25% and the reduction of waste and material costs by up to 90% are some significant achievements, in addition to the main attractiveness of AM processes [6]. Additive manufacturing processes are a promising alternative method to fabricate duplex stainless steels, especially when complex and irregular shapes are required in addition to the density of the materials, in comparison to conventional techniques. However, high cooling rates and control during the processes are of extreme importance to avoid the formation of deleterious secondary phases that can affect mechanical and corrosion-resistant properties.
DSSs have extensive applications as structural materials in many industries and different environments, as these steels present both high mechanical and corrosion resistance properties provided by their dual-phase microstructure (ferrite δ and austenite γ) [6]. Some of their applications involve the chemical, oil, gas, food, and marine industries, where their good performance and attractive, economical cost can substitute alternative materials such as nickel-based alloys. These steels may precipitate undesired intermetallic phases, carbides, and nitrides at different temperatures. Particularly from 600 °C to 1000 °C, the sigma phase (σ), chi-phase (χ), carbides ($M_{23}C_6$, M_7C_3), or nitrides (CrN,

Cr_2N) can precipitate and deteriorate their mechanical properties as well as decrease their corrosion resistance [7]. Moreover, the intermetallic phases present higher content in Fe, Cr, and Mo and, thus, can be the main factor responsible for the decrease in toughness, pitting corrosion, and fatigue characteristics [8-10]. One of the most common nucleation sites for corrosion problems in three-dimensional printed materials is pores. They reduce the passivation property in the presence of sulfuric and phosphoric acid solutions [11]. There are some types of pores: one type exists around un-melted powder particles, and another is caused by the trapped gas inside the powder during gas atomization [1, 12-14]. Porosity can be reduced to a certain extent by optimizing the printing conditions, including laser energy, scanning rate, and scanning direction. It has been found that increasing the laser power or properly decreasing the scanning rate can reduce the porosity of different metals, such as nickel or aluminium-based alloys or some types of stainless steel, such as 316L by LPBF [1, 15].

Corrosion testing of AM components must consider the high degree of anisotropy of all kinds of defects that may appear in such objects, depending on the kind of process. When planning corrosion tests, the correct grinding, and polishing procedures (allowing no modification of the morphology or size of the defects, especially for surface porosity), the surface after post-processing (if applicable), the bulk material-tested surface perpendicular to the build direction (depth is relevant), and the bulk material-tested surface parallel to the build direction must be considered. Not all condition variables will be relevant to corrosion susceptibility under service conditions; however, they may yield valuable information on the kind and distribution of defects in and in the AM material.

Although the influence of corrosion resistance on the microstructure of heat-treated LPBF stainless steel has recently been investigated by a few authors, the sensitivity of post-processed duplex stainless steel to corrosion resistance in sodium chloride solution has not been adequately addressed. The current study evaluates the corrosion resistance of heat-treated super duplex stainless steel in a 3.5% NaCl solution using the potentiodynamic anodic polarization technique and electrochemical impedance spectroscopy (EIS).

MATERIAL AND METHODS

Super duplex stainless steel (SDSS), grade 2507 (EN 1.4410), manufactured by Sandvik Osprey Ltd, with the chemical composition presented in **Table 1**, was used to print square samples (10x10x10mm) in the laser-powder bed fusion (LPBF) process. The SDSS is a gas-atomized powder with particle diameters ranging from 15 to 53 µm.

Table 1 Chemical composition of 2507, EN 1.4410 powder.

Elements	Fe	Cr	Ni	Mo	Mn	Si	N	Cu	C	P	S
[wt. %]	bal.	25	7.0	4.0	<1.2	<0.8	0.30	<0.50	<0.03	<0.035	<0.015

The LPBF printing process was performed on an AM125 RENISHAW printer characterized by a ytterbium (Yb) fiber laser with a maximum laser power of 200 W, a scan speed of 2000 mm/s, and a wavelength of 1.074 nm. The components were manufactured on a mild steel platform under an atmosphere of Ar inert gas at an oxygen level below 10 ppm. A meander scanning strategy was used, following a rotation of 67° after every layer was laid. The following printing parameters were used: laser power P = 180 W, hatch distance h = 120 µm, layer thickness t = 30 µm, and scan speed V = 300 mm/s. The energy density of the applied parameters was calculated according to the formula: Ed = P/(Vht) J/mm^3, and it was 166 J/mm^3.

The super duplex stainless steel SDSS studied in this work was subjected to post-processing heat treatment, and the following three conditions were studied:

- As printed, without any post-processing heat treatment (AS),
- Solution annealing of as printed samples at 1100°C for 15 minutes, fast cooling in water (SA),
- Stress relieving of as printed samples at 300°C for 5 hours, slow cooling with the furnace (SR).

X-ray diffraction (XRD) patterns were collected using an X-Pert PRO instrument. For the X-ray diffraction analysis, a Co target, a scan rate of 0.01 step/s, and a scan range for 2θ between 30 and 120° were used. The X'Pert HighScore Plus was used for phase identification and quantitative analysis. A LEICA MEF4A light optical microscope (LOM) was used for metallographic examination. The metallographic specimens were fabricated using a conventional procedure consisting of grinding, emery paper polishing, and cloth polishing. Samples were then electrolytically etched in 10% oxalic acid, and 3–6 volts were applied for 5–60 s.

Two methods examined the electrochemical properties and characteristics of these materials, namely potent potentiodynamic polarization and electrochemical impedance spectroscopy (EIS). An Atlas 0531EU and IA (Atlas-Sollich, Poland) potentiostat station was put in a 3.5% NaCl solution at room temperature to see if it would corrode. The corrosion tests were performed on the sample's cross-section. Electrochemical tests were carried out in three-electrode corrosion cell systems according to the PN-ISO 17475 standard, with the test sample as the working electrode, an Ag/AgCl reference electrode (potential 207 mV at 25°C), and a platinum wire as the auxiliary electrode. Polarisation tests were divided into the following two stages:

- Determining the open circuit potential (E_{OCP}) over 1 hr.
- Anodic polarization recording of potential changes from E_{OCP} -100 mV with step and potential speed changes of 1 mV/s until a current density of 1 mA/cm2 is reached. The polarity was reversed, and the curve to the initial potential was recorded.

Tafel extrapolation using the AtlasLab software established the characteristic parameters related to electrochemical corrosion, which included current density (J_{cor}), corrosion potential (E_{cor}), and polarization resistance (R_{pol}), which were determined according to the Stern-Geary Equation (1) [16], where and are the slopes of the anode and cathode sections of Tafel, respectively.

$$R_{pol} = \frac{\beta_a + \beta_c}{2.3 \times i_{cor} \times (\beta_a + \beta_c)} \quad (1.)$$

The breakdown potential (E_{br}) was determined as a place of depassivation and the inflection of the anode curve, as well as the method of determining the value of repassivation potential (E_{rp}) as the point of intersection of the return and primary curves.

Electrochemical properties were also determined using the second method, namely electrochemical impedance spectroscopy (EIS), first by stabilizing the samples in the test environment for 15 min without current flow and then with a flow through the solidified AC system at an amplitude of 10 mV at frequencies from 100 kHz to 10 mHz. The results are presented as Nyquist plots. An electrical equivalent circuit (EEC) was assigned to reproduce the relationships appearing in these studies using the AtlasLab and EC Lab software, in which the numerically generated curves were fitted to the experimental results. Apart from typical resistors, non-linear CPEs (constant phase elements) were adopted in the EEC. Two tests per sample were performed in the EIS and potentiodynamic tests. The obtained values were very close to each other; thus, one representative result was selected and presented.

RESULTS AND DISCUSSION

X-ray diffraction and microstructural analysis

As a result of the amazingly fast cooling rate of the LPBF process, the SDSS reveals ferrite as the major phase in the printed samples – as build conditions (**Fig. 1**). The X-ray diffraction pattern in an as-printed state (AS) reveals strong peaks deriving from ferrite phase Fe-α (110), (200), (211) and one weak peak of austenite from Fe-γ (111). Stress relieving heat treatment (SR) does not affect the phase composition (due to the low temperature of 300°C), but the slight increase in the intensity of the main austenite peak Fe-γ (111) can be seen on the X-ray diffractogram. The fully balanced microstructure was formed when the solution annealing (SA) was carried out. In this case, the two phases coexist in almost equal proportions. The peaks deriving from austenite, like Fe-γ (111), (200), (220), (311) and (222) are well visible. The austenite content in as-printed conditions and stress relieving one is 5%, while after solution annealing about 52%.

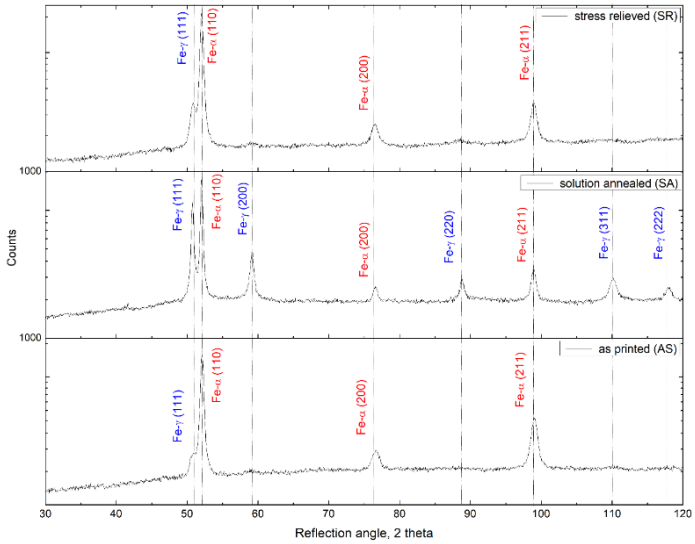

Fig.1 X-ray diffraction patterns for the solution annealed and aged samples.

The microstructure of SDSS in as-printed (AS) condition is present in **Fig. 2**. The microstructure is almost entirely ferritic, with weak austenite only present on the ferrite grain boundaries. The typical microstructural defects were also revealed as non-fully melted powder particles and near-formed cavities. Generally, the ferrite grains are elongated in the build direction. For stress-relieving SDSS, the microstructure was similar. For the solution annealing heat treatment, the balanced microstructure was revealed. The austenite was uniformly distributed between ferritic grains as grain boundary austenite, and intergranular austenite formed inside ferritic grains as Widmanstatten laths (**Fig. 3**).

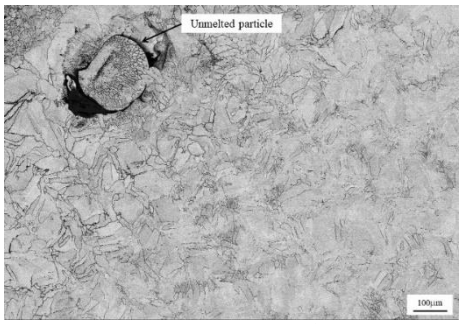

Fig. 2 Shows the microstructure (SEM) of SDSS in as printed conditions (AS), revealing an almost fully ferritic microstructure and structural defect.

Corrosion resistance analysis

The potentiodynamic tests were initiated by the measurement of open circuit potential (E_{OCP}) in a 3.5% NaCl solution (**Fig. 4a**), which was followed by the polarization curve with reverse anodic scan in order to find out the corrosion resistance of LPBF-printed super duplex stainless steel in different sample conditions (Figure 4b). The results of the Tafel analysis of polarization curves are shown in **Table 2**.

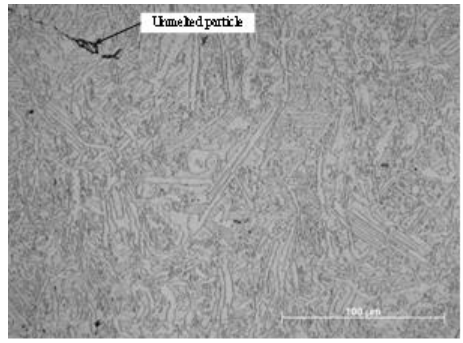

Fig. 3 Shows the microstructure (LOM) of SDSS in solution annealing conditions (SA), revealing a balanced austenite-ferrite microstructure.

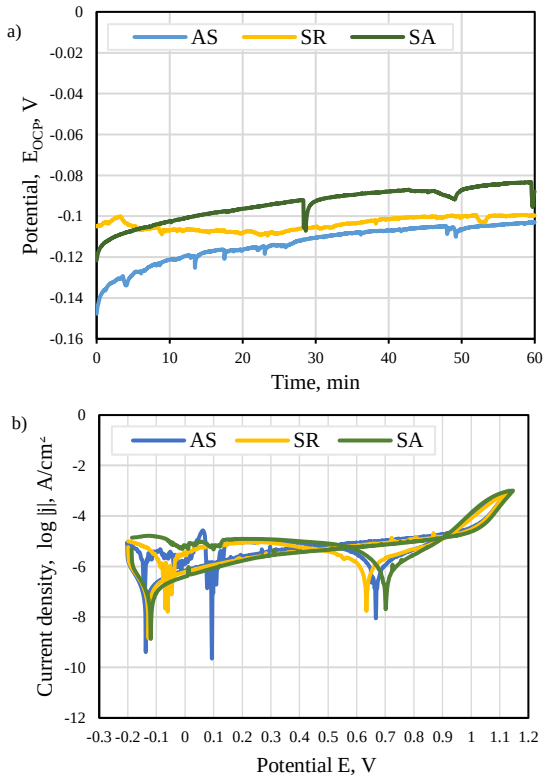

Fig. 4 Electrochemical study results of as printed (AS), stress relieved (SR), and solution annealed (SA) SDSS: a) open circuit potential; b) logarithmic presentation of anodic polarization curves.

Table 2 Potentiodynamic (Tafel analysis) test results of as-printed, stress-relieved, and solution-annealed SDSS.

SDSS condition	E_{br} mV	J_{cor} μA/cm$_2$	β_a mV	β_c mV	E_{cor} mV	R_{pol} Ω*cm^2
As-printed (AS)	1084	140.63	195.73	51.98	-147.17	126.82
Stress-relieving (SR)	1083	166.60	255.88	59.11	-142.86	125.14
Solution Annealing (SA)	1102	131.89	295.36	53.86	-136.35	149.35

The open circuit potential (E_{ocp}) of the studied materials ranged from -148 mV to -105 mV, with greater levels found for solution-annealed samples. In the analysis of the E_{ocp}, the observed rising trend in **Fig. 4a** may be attributed to the presence of its ions at the metal-electrolyte interface in order to produce an equilibrium state [16]. The heat treatment influence on the E_{ocp} values in the solution-annealed conditions was visible. The open circuit potential of SDSS in as-printed conditions grew from -148 to -103 mV, whereas stress relieving resulted in an increase in E_{OCP} from -105 to -99.7 mV. SDSS in all studied conditions shows a shift to positive values of the E_{OCP} during 60 min of immersion in the electrolyte. Higher open-circuit potential indicates slower dissolution reactions of material components and, thus, a slower process of electrochemical corrosion.

The anodic polarization curves of SDSS were determined to have active, passive, and transpassive states. The samples were polarised at 1 mV/s until a current density of 1 mA/cm^2 was reached and then the direction of polarisation was reversed. All the extracted data from the polarization graphs is summarized in **Table 2**. The E_{corr} is a parameter that shows the thermodynamic tendency of a material to oxidation or passivation in a corrosive environment. The lower values of the corrosion potential are related to a higher tendency toward anodic reactions [16]. Therefore, the lower value of the corrosion potential for the as-printed sample confirms that the corrosion reactions initiate more promptly on this sample than on the other samples. The other reason that affects the detection of passivation areas is the concentration of chloride ions (Cl^-) in the test solution. Commonly, the passivation area and the pitting potential on the cyclic potentiodynamic polarization curve are not visible when testing is conducted in solutions with a high (Cl^-) concentration. This behaviour has also been reported for 420 and 430 ferritic stainless steels in solution with higher than 0.5 M Cl^- concentrations [17, 18]. For the studied condition SDSS shows quite stable passive range until breakdown potential (E_{br}). The breakdown potential (E_{br}) and repassivation potential (E_{rp}), which represent the corrosion resistance of materials, were obtained by analysing potentiodynamic curves (**Fig. 4b**). The first represents when surface pitting appears, while the second specifies when additional corrosion damage does not occur. When evaluated as printed and stress-relieved conditions, both potentials were near. The loop formed in the diagram (**Fig. 4b**) was very narrow, with E_{br} = 1090 mV and E_{rp} = 923 mV on average. The repassivation potential (E_{rp}) of all analysed SDSS states was very similar. The

determined characteristic potentials allow it to distinguish the passivity zone, which is apparent in **Fig. 4b** as a segment of the horizontal line after the corrosion potential peak. The commencement can be seen for potentials greater than E_{br}, whereas existing pits were repassivated for potentials greater than E_{rp}. A passage between the E_{br} and E_{rp} potentials is safe for new pits, but those already on the surface may develop.

With increasing AC current density, the passive current density increases, the critical pitting potential shifts negatively, and the passive region gradually narrows. This indicates that the imposed AC can decrease the passivity of 2507 SDSS; that is, the passivation process becomes difficult, which results in an increase in corrosion rate and sensitivity to pitting.

Table 2 demonstrates that the polarization resistance (R_{pol}) decreased significantly for the as-printed and stress-relieved SDSS (from 126.82 Ω cm^2 to 125.14 Ω cm^2, respectively). A delightful outcome turned out for the solution annealed, where the heat treatment enhanced the polarization resistance to 149.35 Ω cm^2. Furthermore, the corrosion current density value (J_{cor}) that is inversely proportional to polarization resistance (R_{pol}) of the stress-relieved sample and as-printed one is higher than that of the solution annealed condition, indicating a higher corrosion rate for the stress-relieving samples. The low current density (J_{corr}) indicates a low corrosion rate or high corrosion resistance [19, 20]. The corrosion current density (J_{cor}) of the stress-relieved SDSS (166.60 μA/cm^2) showed noticeable increase compared to the as-printed conditions (140.63 μA/cm^2), and the biggest difference was recorded for the solution annealed sample treatment, as the corrosion current was 131.89 μA/cm^2.

Electrochemical impedance spectroscopy (EIS) tests were also performed in a 3.5% NaCl solution to characterize the electrical properties and compare the obtained results with anodic polarization curve analysis. An equivalent electrical circuit (EEC) that best describes the corrosion system was fitted to the impedance curves (**Fig. 5**). The EIS results are in good agreement with the EEC's proposal. The EEC model was similar to the study of corrosion evaluation of as-printed and heat-treated 316L stainless steel in a 3.5% NaCl solution [21], as well as the work on the microstructure and corrosion behaviour of a novel additively manufactured maraging stainless steel [22].

$$Z = R_s + 1/(1/R_{ct} + (Y(j\cdot\omega)^{)n} \quad (2.)$$

The EEC consists of a series-connected R-C group, a constant phase element (CPE), and two resistors. The resulting EEC impedance is given by Equation (2). The physical meaning of the EEC proposed [23] is attributed to the electrolyte resistance (R_s), while element R_{ct} corresponds to charge transfer resistance in the phase interface and is inversely proportional to the corrosion rate and surface area being corroded. The constant phase element (CPE_1) is used to describe "capacitance dispersion", which has to do with the capacity of a material's surface area, uneven reaction rates on a surface, and an uneven distribution of current. The results of the EIS analysis are collected in **Table 3**.

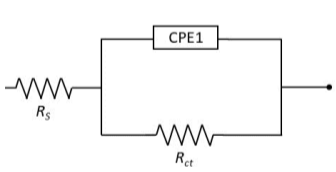

Fig. 5 Equivalent electric circuits (EEC) for materials in NaCl solution

The resistance and capacitance of the electric double layer at the interface of the metal were used to compare the corrosion resistance of each system. The solution annealed SDSS had the most significant differences. The R_{ct} related to the corrosion resistance of the oxide film varied from the lower value (78.34 Ω cm^2) for the as-printed conditions, to 94.80 Ω cm^2 for the stress-relieved conditions, and to 121.50 Ω cm^2 for the solution-annealed SDSS, which has the highest charge transfer resistance. The EIS results indicated almost double the corrosion resistance (based on R_{ct} values) of SDSS in solution-annealed conditions compared to the as-printed one. In the EIS test, the factor n values are slightly below 0.78, probably because they do not present the same uniformity in the passive film of studied conditions. The n value for the solution-annealed conditions is approximately the same as in the study [24] for wrought S32750 grade.

Table 3 Impedance parameters of SDSS in as-printed, stress-relieved, and solution-annealed conditions.

SDSS condition	R_S Ω·cm^2	CPE_1 Y 10^{-6} μF cm^{-2}	CPE_1 n -	R_{ct} Ω·cm^2
As-printed (AS)	7.98	83.61	0.70	78.34
Stress-relieving (SR)	6.95	49.57	0.70	94.80
Solution Annealing (SA)	13.55	70.25	0.77	121.50

The electrochemical results of the Tafel and EIS analysis (**Tables 2** and **3**) show that the solution-annealed SDSS has better corrosion resistance than the other samples because it has the lowest current exchange density. Additionally, heat treatment increases corrosion resistance in impedance tests, which is consistent with previous studies [25]. Due to its increased electrolyte resistance (R_s), the stress-relieved SDSS displayed better corrosion resistance. The high resistance at the point where the electrolyte meets the metal surface and the good corrosion resistance of super duplex stainless steels have mostly been linked to the Cr, Ni, and Mo-rich passive films. This would agree with the proposed model of passive film formation and growth on ferritic, duplex, and austenitic stainless steels [26]. The larger the charge transfer resistance (R_{ct}) value, the better the anti-corrosion resistance. Hence, the 2507 SDSS steel annealed at 1100˚C has the greatest corrosion resistance. The difference in corrosion resistance is closely related to the passive film formed on the stainless-steel electrode. This behaviour is due to the variations in the distribution of the elements in the microstructure during the manufacturing process and subsequent heat treatment. Elements may be homogeneously distributed, forming a single phase, or partitioned in the microstructure; thus, the homogeneity of the oxide film formed over the metallic surface depends on the distribution of the alloy elements and the volumetric fraction of each phase. The non-uniform element distribution will probably favour the formation of a heterogeneous film with different properties at different points.

The SDSS polarisation curves show passive regions with a very similar range in each of the heat treatments tested. Small variations in current density, particularly in the as-printed condition, may be due to nucleation and repassivation of metastable pits, which grow and re-passivate within a few seconds, causing variations in current density that accumulate during the corrosion process.

Based on both corrosion tests, the as-printed SDSS is less resistant to corrosion than the stress-relieved SDSS, but both are far less resistant than the solution-annealed condition. The corrosion resistance of stress-relieved SDSS and solution-annealed SDSS is very comparable. Moreover, it has been observed through research that duplex-phase DSS demonstrates greater pitting potential and repassivation performance in comparison to mostly ferritic structures of DSS produced using LPBF [28, 29].

CONCLUSIONS

The current study evaluates the corrosion resistance of LPBF-printed super duplex stainless (SDSS) steel in 3.5% NaCl solution, subjected to different post-processing heat treatments using the potentiodynamic anodic polarization technique and electrochemical impedance spectroscopy (EIS). Based on the presented results, the following conclusions can be drawn:

- The microstructure of LPBF SDSS in as-printed conditions is almost fully ferritic, with some weak austenite (5%) at the ferrite grain boundaries. A similar structure was revealed for stress-relieving conditions. The microstructure of SDSS after solution annealing is composed of a balanced phase content (52% austenite). Austenite is uniformly distributed between ferritic grains, such as grain boundary austenite, intergranular austenite, and Widmanstatten laths.
- The solution-annealed SDSS in a 3.5% NaCl solution shows a greater open circuit potential E_{ocp} than the as-printed and stress-relieved samples. Heat treatment increased its corrosion potential to more positive values. Solution-annealed SDSS shows improved corrosion resistance at open circuit potential conditions compared to other analysis conditions.
- Based on anodic polarization curves and Tafel analysis, the stress-relieved and as-printed SDSS shows lower corrosion properties than the solution-annealed SDSS. The potentiodynamic data showed lower polarization resistances (R_{pol}) in the stress-relieved state 125.14 Ω cm^2 and 126.82 Ω cm^2 in as printed condition. For the solution-annealed state, an increase of about 20% in polarization resistance was obtained (R_{pol}=149 Ω cm^2).
- Based on EIS results, the solution-annealed SDSS revealed an almost double increase in corrosion resistance (based on R_{ct} values) compared to the as-printed and stress-relieved conditions.
- When the polarization resistance R_{pol} from the Tafel analysis was compared with the charge transfer resistance R_{ct} measured in EIS, in both cases, the solution-annealed SDSS exceeded the corrosion resistance of the stress-relieved and printed conditions.
- Good agreement was revealed between both applied methods of corrosion resistance assessment.
- Stress relieving at 300°C for 5 hours did not affect the corrosion resistance of LPBF printed SDSS, so it can be used without risk of degradation of properties.

Acknowledgments: The research presented in this work was carried out within the framework of the International Visegrad Fund scholarships of Jana Bidulska and Zbigniew Brytan. The research received also support from the EU-project H2020-MSCA no. 823786, i-Weld and international project co-financed by the program of the Ministry of Science and Higher Education entitled "PMW" in the years 2020 - 2023; contract No. 5107/H2020/2020/2.

REFERENCES

1. R. Bidulsky, J. Bidulska, F.S. Gobber, T. Kvackaj, P. Petrousek, M. Actis-Grande, K.P. Weiss, D. Manfredi: Materials, 13, 2020, 3328. https://doi.org/10.3390/ma13153328.
2. T.V. Trinh, S.A. Nguyen, K.G. Pham, C. Seidel, A.H. Pham, C.N. Phung: Acta Metallurgica Slovaca, 29, 2023, 82-87. https://doi.org/10.36547/ams.29.2.1790.
3. R. Bidulsky, F.S. Gobber, J. Bidulska, M. Ceroni, T. Kvackaj, M.A. Grande: Metals, 11(11), 2021, 1831. https://doi.org/10.3390/met1111183.
4. A. Di Schino, G. Stornelli: Acta Metallurgica Slovaca, 28, 2022, 208-211. https://doi.org/10.36547/ams.28.4.1648.
5. Ľ. Kaščák, J. Varga, R. Bidulsky, J. Bidulska, M. Actis-Grande: Acta Metallurgica Slovaca, 29, 2023, 113-118. https://doi.org/10.36547/ams.29.2.1846.
6. R. Colás, G.E. Totten: *Encyclopedia of Iron, Steel, and Their Alloys (Online Version)*, 1st ed., CRC Press: 2016. https://doi.org/10.1081/E-EISA.
7. I. Alvarez-Armas, S. Degallaix-Moreuil: *Duplex Stainless Steels*, John Wiley, and Sons: Hoboken, USA, 2009. https://doi.org/10.1002/9781118557990.
8. T. Tański, Z. Brytan, K. Labisz: Procedia Engineering 74, 2014, 421–428. https://doi.org/10.1016/j.proeng.2014.06.293.
9. N. Sathirachinda, R. Pettersson, S. Wessman, J. Pan: Corrosion Science, 52(1), 2010, 179-186. https://doi.org/10.1016/j.corsci.2009.08.057.
10. S.H. Jang, S.T. Kim, I.S. Leeand, Y.S. Park: Materials Transaction, 52(6), 2011, 1228–1236. https://doi.org/10.2320/matertrans.M2010414.
11. E. Otero, A. Pardo, V. Utrilla, E. Saenz, J. Álvarez: Corrosion Science, 40, 1998, 1421-1434. https://doi.org/10.1016/S0010-938X(98)00047-X.
12. A.L Maximenko, E.A Olevsky: Scripta Materialia, 149, 2018, 75-78. https://doi.org/10.1016/j.scriptamat.2018.02.015.
13. J. Bidulská, T. Kvackaj, R. Bidulsky, M.A. Grande, L. Litynska-Dobrzynska, J. Dutkiewicz: Chemicke Listy, 105(SI4), 2011, s471-s473.
14. J. Bidulská, R. Bidulský, M. Actis Grande, T. Kvačkaj: Materials, 12(22), 2019, 3724. https://doi.org/10.3390/ma12223724.
15. G. Sander, S. Thomas, V. Cruz, M. Jurg, N. Birbilis, X. Gao, M. Brameld, C.R. Hutchinson: Journal of The Electrochemical Society, 164(6), 2017, C250. https://dx.doi.org/10.1149/2.0551706jes .
16. D. Mareci, G.H. Nemtoi, N. Aelenei, C. Bocanu: European Cells & Materials, 10(8), 2005, 1-7. http://doi.org/10.22203/eCM.v010a01.
17. L. Reimann, Z. Brytan, G. Jania: Materials, 15(16), 2022, 5721. https://doi.org/10.3390/ma1516572.
18. M. Finsgar, S. Fassbender, F. Nicolini, I. Milosev: Corrosion Science, 51, 2009, 525-533. https://doi.org/10.1016/j.corsci.2008.12.006.
19. M. Finsgar, S. Fassbender, S. Hirth, I. Milosev: Materials Chemistry and Physics, 116(1), 2009, 198-206. https://doi.org/10.1016/j.matchemphys.2009.03.01.
20. A. Szewczyk-Nykiel, J. Kazior: Journal of Materials Engineering and Performance, 26, 2017, 3450-3456. https://doi.org/10.1007/s11665-017-2778-4.
21. V. Salarvand, H. Sohrabpoor, M.A. Mohammad, M. Nazari, R. Raghavendra, A. Mostafaei, D. Brabazon: Journal of Materials Research and Technology, 18, 2022, 4104-4113. https://doi.org/10.1016/j.jmrt.2022.03.156.
22. S. Ayda, L. Khaksar, A. Nasiri, A. Hadadzadeh, B.S. Amirkhiz, M. Mohammad: Electrochimica Acta, 339, 2020, 135925. https://doi.org/10.1016/j.electacta.2020.135925.
23. H. Xianglong, Q. Ren, Y. Yang, X. Cao, J. Hu, Ch. Zhang, H. Deng, D. Yu, K. Li, W. Lan: Journal of Natural Gas Science and Engineering, 86, 2021, 103718. https://doi.org/10.1016/j.jngse.2020.103718.
24. M. Jafarzadegan, F. Ahmadian, V. Salarvand, S. Kashkooli: Metallurgical Research & Technology, 117(5), 2020, 507. https://doi.org/10.1051/metal/2020048.
25. Ch. Xiaohui, J. Li, X. Cheng, H. Wang, Z. Huang: Materials Science and Engineering A, 715, 2018, 307-314. https://doi.org/10.1016/j.msea.2017.10.002.
26. D. Addari, B. Elsener, A. Rossi: Electrochimica Acta, 53(27), 2008, 8078-8086. https://doi.org/10.1016/j.electacta.2008.06.007.

27. L. Shang, C. Yue, X. Chen, Q. Zhu, Y. Tu: Crystals, 10(4), 2020, 294. https://doi.org/10.3390/cryst10040294.
28. N. Haghdadi, M. Laleh, H. Chen, Z. Chen, C. Ledermueller, X. Liao, S. Ringer, S. Primig: Materials & Design, 212, 2021, 110260.
https://doi.org/10.1016/j.matdes.2021.110260.
29. M. Laleh, N. Haghdadi, A.E. Hughes, S. Primig, M.Y.J. Tan: Corrosion Science, 198, 2022, 110106. https://doi.org/10.1016/j.corsci.2022.110106.